Granular Matter (2021) 23:34
https://doi.org/10.1007/s10035-021-01094-6

ORIGINAL PAPER

The role of the hopper angle in silos: experimental and CFD analysis

David Méndez[1] · **Raúl Cruz Hidalgo**[1] · **Diego Maza**[1]

Received: 5 August 2020 / Accepted: 27 January 2021

Abstract

In this work, we reported experimental and numerical results of granular flows in silos and hoppers. We used a very flexible experimental setup, allowing us to explore the entire domain of the hopper angles. In addition, the granular flow was also studied numerically using Computational Fluid Dynamics. First, the numerical protocol was validated, comparing the output with experimental data of mass flow rate. In general, we obtained a good quantitative agreement between numerical and experimental results using a single set of the model parameters. Remarkably, the numerical results reproduced very well the weak non-monotonic behavior of the mass flow rate dependence on the hopper angle obtained experimentally. Stepping forward, we examined the scaling properties of the simulated velocity $v(r)$ and density $\phi(r)$ profiles at the outlet region. Finally, we also analyzed the velocity and volume fraction field inside the silo. The outcomes suggested that fast dynamics at orifice perturbs the system distinctly, depending on the hopper angle. Interestingly, small and large angles showed a larger zone of influence in comparison with intermediate angles.

Keywords Continuous models · Granular media · Silo flow

1 Introduction

Flows of granulate are commonly found in many engineering's applications and natural process [1]. The following are examples: powder handling, silo discharge, particle conveying, snow avalanches and other large-scale geophysical events like sand dunes [2, 3]. In general, they are complex flows, involving several spatio-temproral scales, ranging from the particle-particle deformation to the container dimensions. Thus, huge experimental and theoretical efforts have been made to understand the macroscopic response of granular media in terms of their local particle-particle interactions [1–3].

The use of continuous phenomenological approaches to describe the macroscopic response of granular media is practically compulsory when dealing with industrial and engineering applications. There are two main reasons for this. On the one hand, the lack of an established analytical framework to explain such complex processes, and the second is the limitation of computers to calculate the individual movement of a vast number of particles, which might be even embedded in a fluid. Since the fifties, researchers have developed continuous models of granular media [4–11], to name a few. Thus, several of them were mainly geared towards study of fluidization (mixtures of solids and gas) [12], trying to adjust to the different types of behavior in the different granular regimes. Under certain conditions, where the control parameter is the mass fraction in comparison with a specific packaging limit, we can consider a granular sample as a gas (collisional regime), a liquid (kinetic regime) or solid (frictional regime -based on soil mechanic theory). Hence, the difficulty of finding a model that works well in all circumstances is challenging, and the complexity of the numerical methods has increased significantly. In fact, the most used models typically have many tuning parameters and require extensive experimental calibration. However, existing experimental methods are still insufficient to calibrate computational methods, especially on the complex scenarios found in industrial applications.

Focused on this issue, the execution and analysis of well-controlled *model* experiments has become a valuable alternative. It typically allows reaching a deeper understanding of those complex flows, addressing the most relevant length and time scales, as well as the microscopic mechanism ruling these processes. Additionally, these results also serve

---

✉ David Méndez
dmendez.3@alumni.unav.es

[1] Dpto. de Física y Mat. Apl., Fac. Ciencias, Universidad de Navarra, 31080 Pamplona, Spain

as useful calibration sets for numerical modeling development [13–20]. A silo discharge is a paradigmatic example of granular flows [21–30]; in this work, we use it as a *model* experimental system.

In the past, to predict the mass flow rate of a silo W, as a function of the orifice size has been attempted, but not consummated yet. Moreover, a theoretical formulation linking the value of W with the flow micro-mechanical details is also lacking. Much less is known about cylindrical and rectangular hoppers, where the hopper angle also plays a significant role. In the next paragraphs, we summarize several theoretical formulations, which are used further in the discussion.

1.1 Mass flow rate correlations

Five decades ago, Beverloo et al. [21] introduced a popular phenomenological formula, which describes the correlation between the mass flow rate W in a silo and its outlet size $D = 2R$. It reads as:

$$W = C\rho_B\sqrt{g}(D - kd)^{5/2} \tag{1}$$

where $\rho_B = \rho_M\phi_B$, and ρ_M is the material density of the grains, ϕ_B is the solid-fraction, while C and k are fitting constants. The formulation of Eq. (1) rests on the assumption that the velocity of the grains at the exit scales with the outlet size as $\sqrt{D}$. The fitting parameter C accounts for the macroscopic mechanical response of the specific material, while $(D - kd)$ is the effective size of the orifice when considering grains of dimension d.

Almost at the same time, Brown and Richards [31] developed a theoretical framework based on the concept of *minimum energy theory*. From their analysis, they proposed an expression relating the mass flow rates in a conical hopper with the angle α.

$$W(\alpha) = W_{90^\circ}\frac{\left(1 - \cos^{\frac{3}{2}}\alpha\right)}{\sin^{\frac{5}{2}}\alpha} \tag{2}$$

where W_{90° correspond to the flat bottom limit. Interestingly, Eq. (2) suggests that in similar conditions (particle size and local friction), the mass flow rate $W(\alpha)$ shows a non-monotonous behavior when increasing the hopper angle.

Some years ago, the silo discharge in 2D and 3D was examined [24, 25], and an alternative quantification of the mass flow rate $W(D)$ in terms of the outlet size $D = 2R$ was introduced [24, 25]. This formulation assumed that the vertical velocity $v_z(r)$ and solid-fraction $\phi(r)$ profiles, at the silo exit are self-similar functions of r/R, when their values are scaled with the values at the orifice center v_c and ϕ_c, respectively. Very recently, this idea has been tested for the case of 2*D* hoppers by J. Darias et al. [32], assuming that

$$\frac{v_z(r)}{v_c} = \left(1 - \left(\frac{r}{R}\right)^2\right)^a \tag{3}$$

$$\frac{\phi(r)}{\phi_c} = \left(1 - \left(\frac{r}{R}\right)^2\right)^b \tag{4}$$

where the value of the exponents a and b mainly govern the shape of the scaled curves. The novelty of Ref. [32] approach was to introduce a characteristic velocity, $v_c = \sqrt{2\gamma gR}$ controlled by an angle-dependent $\gamma(\alpha)$ coefficient, which quantifies the impact of the hopper angle α on the vertical acceleration profiles $a_z(z, \alpha)$.

Following the procedure introduced in Ref.[25], and given the hopper angle α, the coefficient $\gamma(\alpha)$ reads as:

$$\gamma(\alpha) = \int_{\infty}^{0} \frac{a_z(z, \alpha)}{g}\frac{dz}{R}. \tag{5}$$

In reference [32], the previous ideas have been discussed thoroughly. Thus, the 2D experimental data showed that the rest of the parameters (in Eqs. (3) and (4)) have a smooth dependence on α. Meanwhile, the specific values of a and b mainly defined the curvature of each profile, and showed the same trend when decreasing α: the smaller the hopper angle, the flatter the profiles were. Moreover, the impact of α on the solid-fraction was only relevant for small orifice apertures. The authors argued that to assume this functional dependence $\gamma(\alpha)$ and $v_c = \sqrt{2\gamma(\alpha)gR}$, led to an angle-dependent volumetric flow rate $W(\alpha)$, which is equivalent to the Brown & Richards formulation of Eq.((2)).

Based on the previous 2D approach, here we test it in the case of 3D cylindrical hoppers where the flow rate results,

$$W = \int_0^R \int_0^{2\pi} \rho_M\phi_c(R)\, v_c(R)\left[1 - \left(\frac{r}{R}\right)^2\right]^{a+b} rd\varphi dr. \tag{6}$$

Note that the factorization of the particle flux as $\mathbf{P}(r) = \rho_M\phi(r)\mathbf{v}(r)$ and the azimuthal symmetry are the only assumptions. Substituting (3) and (4) in (6), and integrating, it results in a closure formulation of W in terms of $\gamma(\alpha)$, the shape parameters a and b and $\phi_c(R)$. Thus, $W(R)$ reads as,

$$W(R) = \pi\rho_M\sqrt{2g}\left[\frac{\sqrt{\gamma}\phi_c(R)}{1 + a + b}\right]R^{\frac{5}{2}} \tag{7}$$

Remark that Eq. (7) have been derived only assuming the self-similar properties of the velocity and density profiles at the orifice, and that the exit velocity scales as $v_c(R) = \sqrt{2g\gamma R}$. Besides, it also accounts for the significant dilatancy of the material near the outlet. Notably, the derivation is done without including any artifacts, such as the existence of an *empty anulus*, which is commonly used when examining Beverloo's correlation.

In the next sections, we present a detailed experimental and numerical analysis regarding the applicability of the phenomenological formulation Eq. (7), when varying the angle of the hopper α. The paper is organized as follows: in Sect. 2, the experimental set-up is described, and the obtained values of mass flow rate W, resulting for different hopper angles and outlet sizes $2R$ are summarized. In Sect. 3, the numerical model is explained in detail. Section 4 exposes the data corresponding to the flat silo, which allowed to calibrate of the relevant parameters of the numerical tool. Besides, it also discusses numerical data corresponding to hoppers with a fixed orifice radius, but different angle α. We contrast the $W(\alpha, R)$ outcomes obtained experimentally with their numerical counterparts, and performed a scaling analysis to deduce the parameters of the phenomenological formulation Eq. (7). Finally, the attention is focused on the kinematic fields inside the silo.

2 Experimental procedure

Our model experiment is a lab size cylindrical silo with a series of interchangeable hoppers at its base. The cylindrical container has an inner radius of $R_s = 8.65$ cm, and is made in 0.3 cm thick Plexiglas. The container is filled with monodisperse Glass beads, $d = 0.1$ cm diameter. Different hoppers made in PLA by 3D printers can be adjusted in the base by a adjustable vertical-sheets frame to guaranty the setup integral rigidity, and all the setup is located on an elevated plate, see Fig. 1a. Under it, a computer-controlled weight-scale measure the mass discharged by the hopper. A home-made software records the output data over time with a 0.5 s resolution. The mass versus time signals grow linearly on time for all the explored parameters, and accordingly, the mass flow rate, $W(\alpha)$, is obtained by its linear fit (see Fig. 1b).

Complementarily, while the particles flow out from the silo, an ultrasonic position sensor measures the material free surface position $z(t)$, simultaneously. Then, a linear fit of the position versus time (see inset of Fig. 1c) provides the velocity of the top surface, $v_s(\alpha)$. Assuming the continuity law is valid, $W(\alpha) = \rho_b \pi R_s^2 v_s(\alpha)$, the measurements of $W(\alpha)$ and $v_s(\alpha)$ varying α, can be used to estimate the granular material bulk density, ϕ_b. Fig. 1c shows $W(\alpha)$ versus $v_s(\alpha)$. Data slopes then provide the bulk solid-fraction, which characterizes the bulk solid-fraction for our experiences, $\phi_b = 0.62 \pm 0.02$.

The flexible design of our model experiment and its accuracy are remarkable. It allow us to examined hoppers of nine different tilt angles, ranging $\alpha = 90°$ to $\alpha = 10°$. Checking the data values (see Table 1),it is evidenced that the flow rate versus angle dependence is non-monotonous, and small hopper angles imply discharge rates lower than the one corresponding to flat bottom silos. Beyond this observation, discussed in detail in the next sections, the discharge rate is stationary even when only the hopper region is empty.

3 Numerical model

The Fig. 2 illustrates the numerical model, which consists in a cylindrical container of height h and radius R_s. At the bottom, it ends in a hopper with an internal angle of α (measured respect the vertical) and a exit aperture radius, R. Here, we examine hoppers with outer angles of the cone, ranging from $\alpha = 90°$ to $\alpha = 10°$. Note that $\alpha = 90°$ represents a flat silo.

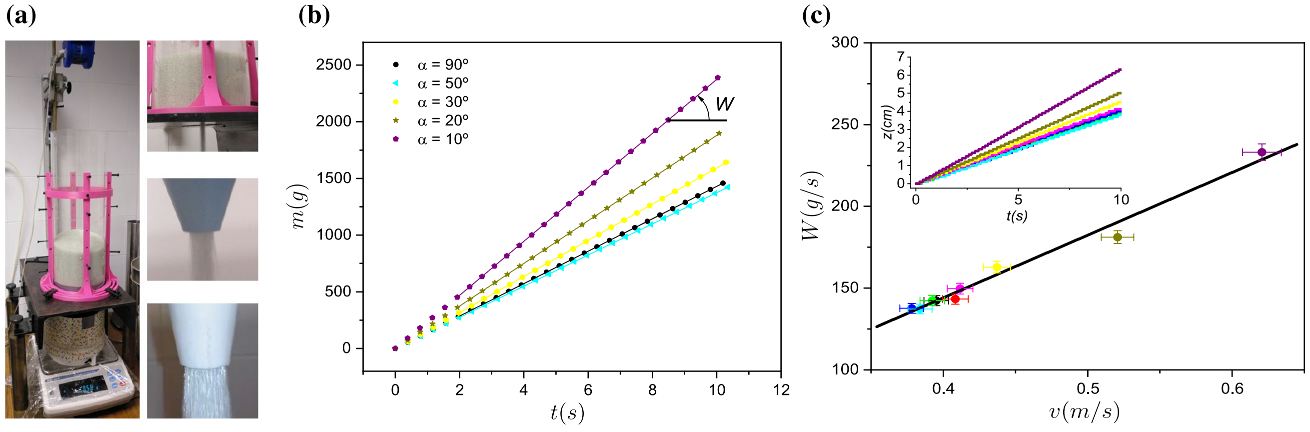

Fig. 1 **a** The experimental setup: a base (B) support different hoppers(H) that discharge the material in a calibrated weight-scale (W). A ultrasonic sensor (U) determines the free surface position. **b** Temporal evolution of the mass discharged by silo by the different hopper angles studied in this work. **c** Mass flow rate against the free surface velocity, obtained from the temporal evolution of the free surface position (inset). Linear fit slope provides an indirect measurement of the bulk solid-fraction

Table 1 Experimental data of mass flow rate of silo and hoppers, obtained for different hopper angles and $R = 10mm$ (W, standard deviation, σ and the ratio $\frac{W}{W_{90}}$)

α (o)	W (a) g/s	W (b) g/s	W (c) g/s	Mean g/s	σ g/s	$\frac{W}{W_{90}}$
90	142.16	142.86	141.97	142.33	0.47	1.00
80	143.35	142.16	144.47	143.33	1.16	1.01
70	141.62	142.05	143.67	142.45	1.08	1.00
60	137.57	137.32	138.12	137.67	0.41	0.97
50	137.25	137.26	137.25	137.25	0.01	0.96
40	147.6	149.62	151.86	149.69	2.13	1.05
30	160.96	163.76	163.86	162.86	1.64	1.13
20	182.8	180.33	180.39	181.17	1.41	1.32
10	241.43	237.62	238.19	239.08	2.06	1.68

We use the academic version of Ansys Fluent 19.2 [33] to simulate our experimental setup. It is a continuous approach that combines the momentum balance equation with phenomenological granular constitutive laws inspired on the kinetic theory of granular flows (KTGF) [12]. Currently, Ansys Fluent includes more elaborated formulations, which can handle dense granular systems [34, 35]. Here, we explore the feasibility of this numerical tool, describing the hopper flow.

The model includes two-phases (gas and solid), where each phase can occupy each point of the space in any proportion, given by its local solid-fraction $\phi(\mathbf{r})$. For simplicity, in our calculation, the drag force between the particle and the interstitial air is not considered, and consequently, solid and gas phases are decoupled. In the following, we describe the theoretical framework concerning the solid phase, briefly.

Under these conditions, particles behave as a gas with inelastic collisions, moving in a given region of the space limited by walls. KTGF approach assumes that particles collide in binary inelastic collisions and that their speed distribution is a Gaussian [12]. From that point, 3D singular constitutive equations are deduced for the kinetic and collisional regimes.

Typically, these granular constitutive laws includes shear $\eta_s(\mathbf{r})$ and bulk viscosities $\eta_b(\mathbf{r})$, arising from the mechanisms of particle momentum exchange. The bulk viscosity $\eta_b(\mathbf{r})$ quantifies the resistance of the system to compression and expansion, and it mainly depends on the particle restitution coefficient e_n, the local solid-fraction $\phi(\mathbf{r})$ and granular temperature $\Theta(\mathbf{r})$ [8]. On the other hand, the shear viscosity $\eta_s(\mathbf{r}) = \eta_c(\mathbf{r}) + \eta_k(\mathbf{r})$ accounts for several shear resistance sources, depending on the specific type of behavior (collisional and kinetic). Both, the collisional and the kinetic shear viscosities also depend on e_n, $\phi(\mathbf{r})$ and $\Theta(\mathbf{r})$, mainly [12]. Moreover, to obtain more realistic outcomes, the model also includes an additional source of shear viscosity [36], which is called frictional viscosity $\eta_f(\mathbf{r})$ that mimics the role of the macroscopic Mohr-Coulomb friction angle α_f of the specific material. It is worth to mention $\eta_f(\mathbf{r})$ is very relevant when modeling systems densely packed [36]. When stating the shear frictional viscosity η_f, the solid pressure $P_s(\mathbf{r}) = P_k(\mathbf{r}) + P_f(\mathbf{r})$ is also an important ingredient, and it involves the kinetic-collisional pressure $P_k(\mathbf{r})$, and the frictional pressure $P_f(\mathbf{r})$.

In principle, the formulation of the kinetic-collisional pressure $P_k(\mathbf{r})$ is an outcome of the original KTGF, where the particle restitution coefficient e_n plays a significant role. However, the original KTGF only accounts for the collisional dissipation, due to normal collision between particles. Here, we use the formulation of S. Chialvo and S. Sundaresan [37], that also comprises for the tangential collisional dissipation, introducing an effective restitution coefficient e_f defined as,

$$e_f = e_n - \frac{3}{2}\mu e^{-3\mu} \tag{8}$$

where $\mu = \tan(\alpha_f)$ is the particle friction μ and e_n is the normal restitution coefficient.

Nevertheless, the nature of the frictional pressure $P_f(\phi)$ rests on the strength of the particle-particle contacts. Accordingly, it depends on the local solid-fraction $\phi(\mathbf{r})$, strongly. When the solid-fraction is low the $P_f(\phi)$ practically diminishes, but it should diverge at an upper limit, given the hard particle approach. In particular, in our calculation we use the Johnson and Jackson formulation for $P_f(\phi)$ [38], which read as,

$$P_f(\phi) = \begin{cases} \frac{\phi}{10}\frac{(\phi-\phi_{min})^2}{(\phi_{max}-\phi)^5} & \phi > \phi_{\mathrm{min}} \\ 0 & \phi \leq \phi_{\mathrm{min}} \end{cases} \tag{9}$$

and it involves several parameters as the packing limit ϕ_{max}, *i.e.* the maximum solid-fraction that the model is able to handle. Besides, in Eq. (9) the frictional packing limit ϕ_{min} represents a solid-fraction threshold, above which the frictional viscosity is included. To avoid the numerical divergence of the frictional pressure Eq. (9), the simulation began from an initial condition, defined as an homogeneous system with packing fraction $\phi_0 = 0.6$. Thus, the contribution of the frictional viscosity is practically not included during the first iterations. However, latter on, while the numerical procedure converges, the volume fraction increases towards the stable solution. In all cases reported here, the volume fraction in the bulk region resulted in $\phi \approx 0.61$ in steady state conditions.

When modeling granular flows using continuous approaches, the specific boundary conditions are essential, because they determine the energy lost due to the inelastic collisions between the particles and the walls The system modeled here has fixed walls; the normal momentum transfer is modeled using a Jhonson and Jackson formulation [38] and following [39–41], with an algebraic form of the granular temperature, where convective and diffusive terms are neglected. Shear momentum transfer from the solid phase to the wall is quantified through a specularity parameter κ, which ranges from zero to one. When κ is zero, the shear at the wall surface is zero. On the opposite side, $\kappa = 1$ mimics a significant lateral momentum transfer to the wall. In all simulations presented here, we have used $\kappa = 0.1$.

Once the formulation of granular constitutes behavior and the boundary conditions are prescribed, the solver integrates the transport processes of mass, momentum, and energy at unison. Thus, starting from a discretized domain, the transport equations are integrated for all the cells that compose the system. In particular, the velocity fields result from the momentum conservation law and the continuity law, using an implementation called PC-SIMPLE (Phase Coupled Semi-implicit Method for Pressure Linked Equations). This procedure begins from a prescribed pressure that changes iteratively until the continuity equation is satisfied. The values of momentum, solid-fraction, and temperature at the faces are determined using a First Order Upwind Scheme, where the values at the faces equal the value of the upper cell (upstream cell). However, a second-order scheme (validated for multiphase systems) addresses the pressure values at the faces. In all cases, the gradients are evaluated through a Least Squares Cell-Based Gradient Evaluation, assuming a linear variation between adjacent cells. The time dependence is introduced by a Non-Iterative Time Advancement Scheme, which is very efficient and accurate enough [33, 42].

As we mentioned earlier, the simulated system consists in a cylinder with radius $R_s = 8.65$ cm ending in a hopper. Specifically, we used a set of parameters to mimic spherical glass particles with $r_p = 0.05$ cm, which are driven by the gravitational field and leave the container through a bottom circular outlet several radius for flat bottom silo and angles for hoppers. We explore different mesh configurations until velocity and vertical acceleration profiles become almost independent of the mesh size. All the relevant parameters of the model are summarized in Table 2, and in all cases the presented data correspond to steady state conditions.

Table 2 Inputs to the CFD code Ansys Fluent

Inputs granular model	Value
Particle diameter (d_p)	0.001
Particle-Particle restitution coefficient (e_n)	0.97
Frictional Packing Limit (ϕ_{min})	0.52
Packing limit (ϕ_{max})	0.63
Angle of internal friction α_f	30°
Effective Restitution Coefficient e_f	0.8
Specularity coefficient κ	0.1

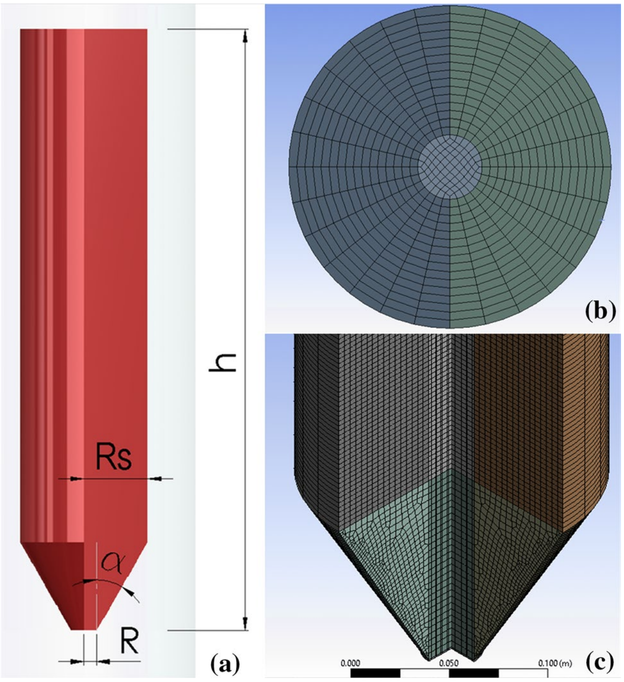

Fig. 2 Model geometry (**a**), top (**b**) and 3D view, (**c**) of the mesh

4 Results and discussion

4.1 Flat silo configuration

As starting point, we discuss results corresponding to flat bottom silos ($\alpha = 90°$). The analysis consisted in examining the correlation between the mass flow rate W and outlet size R. We performed systematic measurements, accounting for the amount of particles flowing out from the silo. The micromechanical origin of this dynamics was explored in [25] by a DEM numerical approach, but here, CFD simulations were implemented to mimic the particle discharge process.

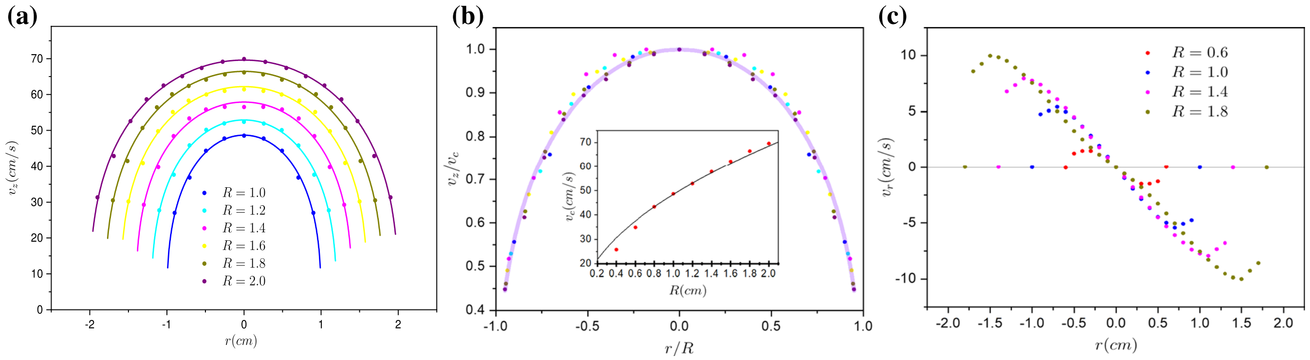

Fig. 3 Velocity profiles at the silo exit. **a** Vertical velocity, $v_z(r)$, for different holes of radius, R taken in a horizontal line in the orifice. **b** Normalized velocity data vs r/R. The continuous lines is the best fit of Eq. (3). **c** Radial velocity profiles, $v_r(r)$, for different holes of radius, R, against the horizontal coordinate r at the orifice

First, our attention was focused on the velocity and solid-fraction fields near the orifice region. Figure 3 shows the numerical data of the radial profiles $v_z(r)$ and $v_r(r)$, namely vertical and radial velocities, obtained in the region of the orifice for several exit sizes. For $v_z(r)$ (see Fig. 3a), we found that the curves have the same shape, as the obtained in quasi-2D experiments [24] and 3D DEM simulations [25, 43]. In the figure, each data series was fitted using Eq. (3), using the velocity at the center v_c and the exponent a as fitting parameters. Remarkably, the velocity values corresponding to different aperture sizes collapsed, when normalizing them by $v_c(R)$ and the radial coordinate was rescaled with R (see Fig. 3b). The scaled data can be fitted with a single exponent $a = 0.35$, which is a bit lower than the reported for 2D and 3D silos. Besides, the values of $v_c(R)$ displayed in the inset can be fitted by the expression $v_c(R) = \sqrt{2\gamma g R}$ with a value of $\gamma = 1.2$. The behavior of the radial velocity $v_r(r)$ is examined in Fig. 3c. Interestingly, except near to the border of the orifice, the profiles of $v_r(r)$ resulted almost linear for all the explored orifices. Furthermore, all the curves had a very similar slope regardless the R value, indicating that the size of the orifice does not play any significant role determining the velocity gradient in the radial direction.

Figure 4 shows the vertical profiles of the convective acceleration on z-axis, $a_z(z)$, obtained for flat silos with different orifice sizes R. Note, all the curves collapsed when the vertical coordinate was scaled with R and the values of acceleration were normalized with g. The scaling indicates that R is the most relevant length scale controlling the magnitude of the velocity gradients at the orifice region. Thus, our outcomes obtained using a computational fluid dynamics framework resulted fully consistent with the assumption that $v_c = \sqrt{2\gamma g R}$ introduced in [25]. Complementarily, the inset of Fig. 4 shows the data of γ obtained using Eq. (5) in comparison with the global γ parameter used to fit v_c in Fig. 3b. The concordance between the results is noticeable.

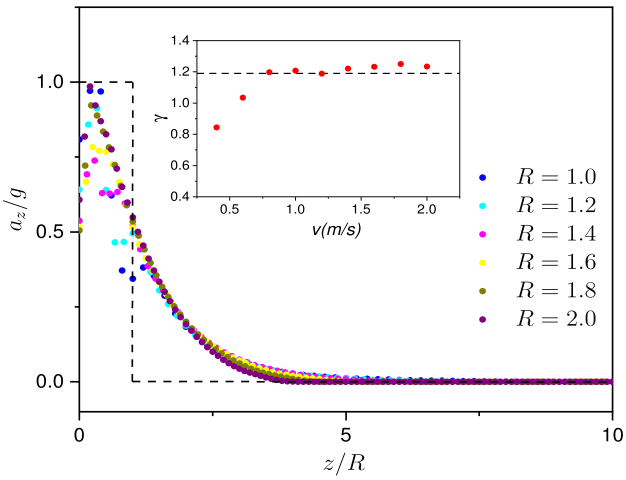

Fig. 4 Vertical profiles of the vertical acceleration $a_z(z/R)/g$ normalized with g, obtained for different orifice sizes R, the data correspond to a region $\Delta r =$ centered at the orifice. The inset illustrates the estimation of γ using Eq. (5) in comparison with $v_c^2/(2gR)$

Aiming to rationalize the spatial density changes, Fig. 5 shows the solid fraction radial profiles $\phi(r)$, obtained for the entire range of explored outlet sizes R. Clearly, the profiles are flatter than their vertical velocity counterpart $v_z(r)$ (see Fig. 3a). More importantly, the solid fraction values at the orifice center ϕ_c resulted significantly lower than the value obtained inside the silo. Although the scaling quality is not as good as the velocity one, the shape of the curves is very similar. Using Eq. (4) the parameter $b = 0.1$ allows fitting all the scaled data with reasonable accuracy . Remarkably, the dependence of solid fraction at the orifice ϕ_c on R (see Fig. 5b) resulted in good agreement with the expression introduced in Mankoc et al. [22]:

$$\phi(R) = \phi_\infty[1 - \alpha_1\, e^{-\alpha_2 R}] \tag{10}$$

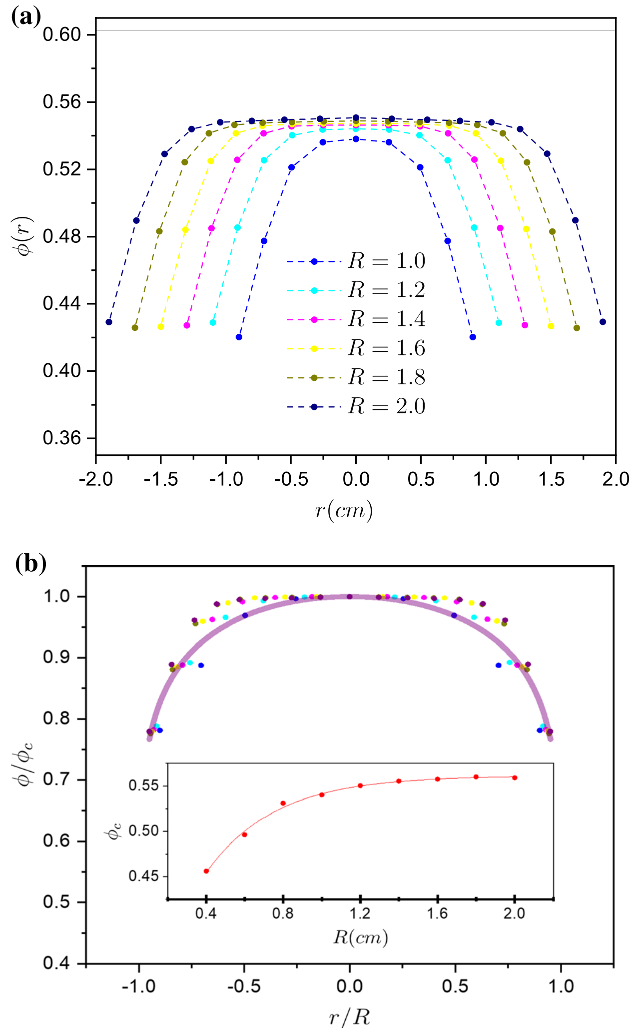

Fig. 5 (a)Solid-fraction profiles, $\phi(r)$, for different orifices, R taken in a horizontal line in the orifice. The dashed line indicates the assigned bulk solid fraction. (b) Normalized solid-fraction profiles, ϕ/ϕ_c and (inset) evolution of the maximum of the solid-fraction profile, ϕ_c, respect the hole radius, R. The continuous line is the best fit of Eq. 10

using $\phi_\infty = 0.561 \pm 0.002$, $\alpha_1 = 0.578 \pm 0.045$ and $\alpha_2 = 0.358 \pm 0.025$. The latter indicates that even at the infinite limit of R, the solid fraction at the orifice region would result significantly lower than the bulk value inside the silo.

Focusing on the mass flow rate data W, Fig. 6 compares experimental results with their numerical counterparts. The graph includes experimental and numerical data, and the analytic output obtained form the scaling arguments Eq. (7). Beyond the excellent agreement between experimental and numerical observations, the full range of results is also well described using Eq. (7). Such agreement validates the use of the parameters ($\gamma = 1.2$, $a = 0.35$ and $b = 0.1$), when determining the numerical prefactor of the mass flow rate expression Eq. (7).

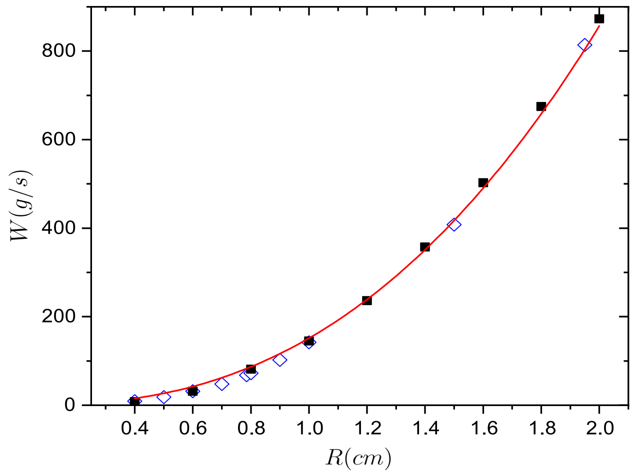

Fig. 6 Mass flow rate obtained experimentally (empty diamond) and numerically (black squares). The error bars are under the symbol size. Continuous line correspond to Eq. (7) (see text for details)with $a = 0.35$ and $b = 0.1$

In the end, a single set of parameters for the Ansys-fluent solver allowed us to reproduce the experimental results with good quality. In the next section, they were used as a reference framework, addressing the role played by the hopper angle on the outflow from a silo..

4.2 Hopper with different angles

As a second step, experiments and numerical simulations were carried out, exploring hoppers with a fixed orifice radius $R = 1$ cm and varying the hopper angle α from 90∘ to 10°. Note that $\alpha = 90°$ recover the limiting case of a flat silo. Again, the experimental system allowed us to measure the flow rate accurately, and simulations of the real set-up performed. As mentioned in Sect. 4.1, all the relevant parameters of CFD scheme were calibrated for the flat bottom limit. Then, it allows us to explore hoppers systematically, changing the hoppers angle. Figure 7a illustrates the vertical velocity profiles $v_z(r)$ obtained numerically for different angles of the hopper. For clarity reasons, in each case, the values are rescaled with the velocity at the center of the orifice v_c. It is noticeable that as the angle increases, the profiles get flatter, denoting that the shear rate values reduce notably in comparison to the flat silo case. The limiting case $\alpha = 0°$ would correspond to a *plug flow*, where the velocity profile is almost uniform. In all cases, the data values fit very well with Eq.(3), using v_c and the exponent a as fitting parameters, and the results are represented with continuous lines.

Figure 7b shows the dependency of v_c with the hopper angle α. Note, that when α is large, *i.e.* getting closer to the flat silo limiting case, the velocity at center showed a weak non monotonous trend. When approaching to the opposite limit, however, v_c increased notably with diminishing α.

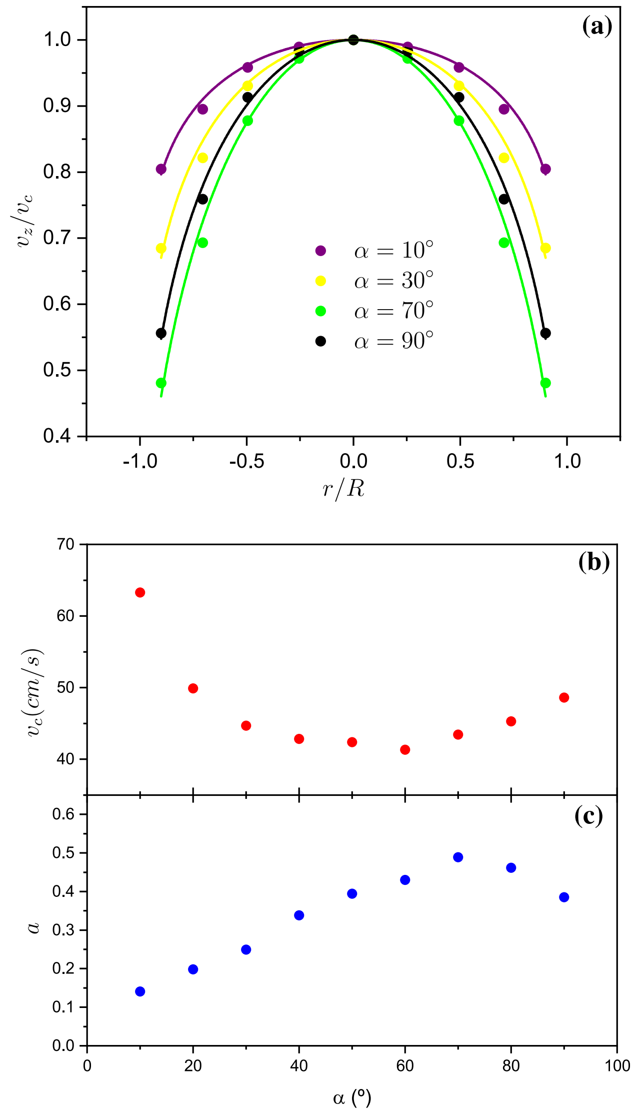

Fig. 7 **a** Normalized velocity profiles, $v_z(r)/vz(0)$ obtained for different hopper angles α. In **b** velocity at the center of the orifice $v_c = v_z(0)$ as function of the hopper angles α, as well as, the corresponding values of the exponent a

Here, one could argue that in concordance with the momentum balance, and assuming steady state conditions, this trend indicates the enhancing of the stress gradient (up-down) with decreasing the hopper angle α. Figure 7c illustrates our estimation of the parameter a, obtained when varying α. The value of a seems to increase towards 0.5, while approaching the flat silo limiting case, but the trend fails close to $\alpha = 90°$. Reducing the frictional packing limit ϕ_{min} (see Eq. (9)), this inconsistency smooths out. However, this change also significantly impacts the discharge rate dependency on the hopper angle α. Therefore, we assume this weakness in our analysis. In the next section, we discuss this fact when analyzing the impact of the hopper angle on the mass flow rate W.

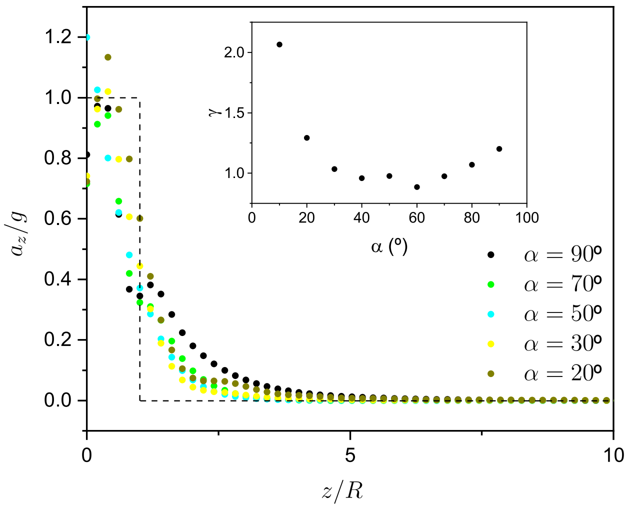

Fig. 8 Normalized profiles of vertical acceleration $\frac{a(z/R)}{g}$ for different hopper angles, α, taken in a vertical line centered in the orifice.The dashed line represent the ideal *free fall arch* limit. Inset: γ factor corresponding to each hopper angle (see Eq. (5))

Figure 8 illustrates, the convective acceleration profiles on the vertical direction $a_c(z)$, resulting for different α. As can be expected, the $a_c(z)$ profiles could not be scaled with the orifice size R, denoting a strong dependence of γ when changing α. This statement is proven by the numerical integration of the profiles (see Eq. (5), which is plotted as a function of α in the inset of Fig. 8. Clearly, the γ's dependence on the hopper angle is non monotonous. This fact is related with the differences in vertical accelerations profile, which are a consequence of the hopper influence on the vertical stress propagation.

Figure 9a illustrates the solid-fraction profiles $\phi(r)$ obtained numerically for different angles of the hopper. For clarity reasons, in each case the values are scaled with the solid-fraction at the center of the orifice ϕ_c. We detected a significant impact of α on the shape of the profiles. The curves indicate that the profiles get flatter and the density gradients vanish, when decreasing α. Figure 9b shows the behavior of ϕ_c when changing α, denoting the non-significant role played by α, determining the value of ϕ_c at the orifice. Contrary, we found that b rises smoothly as the hopper angle increases, but the largest observed value is still lower than the reported for 2D and 3D silos (see Fig. 9c). As mentioned earlier, near the exit, the material solid-fraction tends to be uniform when decreasing α.

At this point, our numerical outcomes conclusively indicated that the hopper angle α controls the shape of the velocity and solid-fraction profiles at the exit. Figure 10 focuses on the impact of α on the mass flow rate $W(\alpha)$, comparing the experimental and numerical results of $W(\alpha)$, as well as, the result of the scaling analysis of the kinematic fields

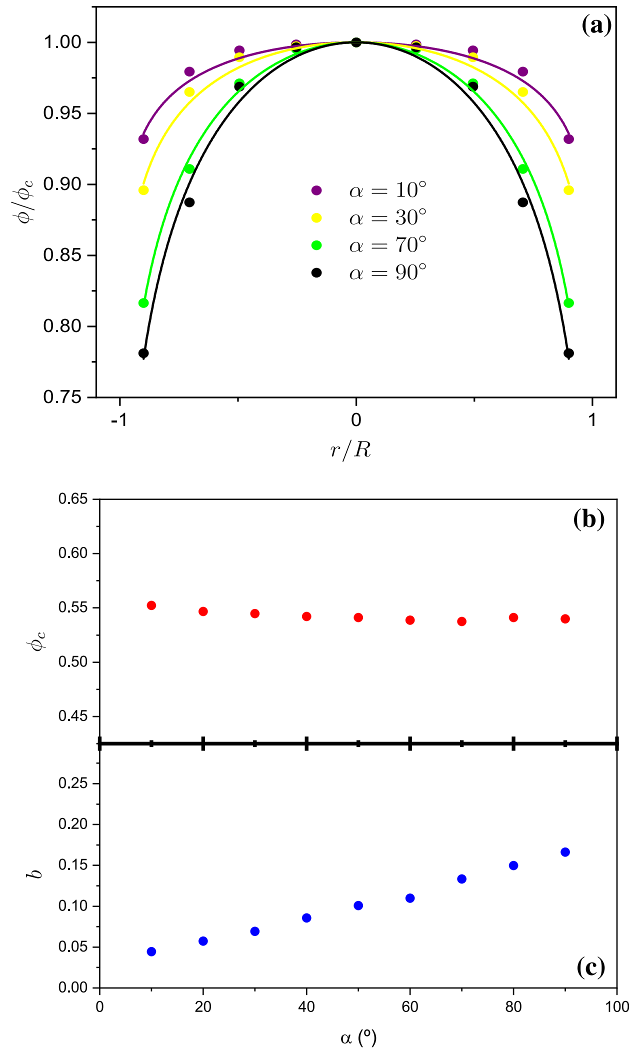

Fig. 9 In **a** the spatial solid-fraction profiles $\phi(r/R)$ obtained for different hopper angles α. In **b** solid-fraction at the center of the orifice $\phi_c = \phi(0)$ as function of the hopper angles α, as well as, the corresponding values of the exponent b (**c**)

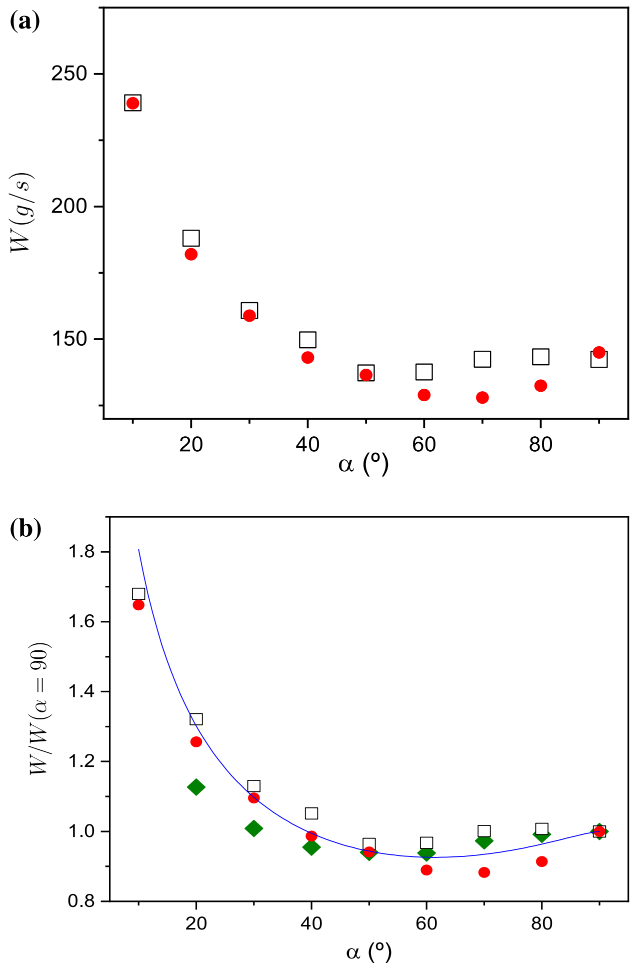

Fig. 10 In **a** Mass flow rate dependence on the hopper angle. Experimental data (empty squares) and its numerical counterpart (red circles). In **b** the comparative evolution of the normalized mass flow rate, $W/W_{90°}$ and an alternative set of parameters (green diamonds) has also included. The continuous line is the analytical prediction of Brown and Richards [44]

at the orifice Eq. (7). Remarkably, it is noticeable that the used CFD numerical tool reproduced the experimental outcomes with reasonable accuracy, Moreover, several relevant observations can be extracted from these results. The first, as expected the hopper angle also controlled the values of $W(\alpha)$, which rises abruptly while approaching to the case of a granular pipe flow ($\alpha = 0$). The second is the fact that $W_{60°}$ and $W_{50°}$ resulted lower than $W_{90°}$ (flat silo limit), which pointed out to a nonmonotonic behavior of $W(\alpha)$. Back in the sixties, this nonmonotonic feature was analytically predicted by Brown and Richards (see Eq. (2)). Note this prediction was founded in mass conservation arguments, linked with symmetry constraints that are imposed on hopper flows. Although their analytical predictions overestimate the resulting flow rate, their phenomenological discharge rate dependence on the hopper angle (see Eq. (2)) shows a nonmonotonic behavior. The experimental results displayed in Fig. 10 are consistent with this observation, and a slight increase in the flow rate with the angle is visible, for $\alpha > 50°$ while approaching the flat silo limit. Note that the used numerical tool and the flow rate Eq. (7) derived from the scaling analysis of the kinematic fields at the orifice also reproduced this nonmonotonic feature, denoting the consistency of our outcomes. Indeed, the numerical results are in excellent agreement with Brown and Richards' solution, as shown in the inset of Fig. 10. To execute this comparison, the data values were normalized with $W_{90°}$, *i.e.* the flow rate obtained in the flat silo limit.

Nevertheless, using the reported set of parameters (see Table 2), deviations were evident for large hopper angles (see Fig. 10a). Complementarily, Fig. 10b also includes the numerical solution corresponding to an alternative set of parameters ($\phi_{min} = 0.57$ $\phi_{max} = 0.62$ and $\kappa = 0.2$, the rest the same). This new set provided an excellent agreement with the experimental results when simulating large hopper angles $\alpha > 50°$. Unfortunately, the numerical algorithm was unstable or underestimated the experimental results for small angles significantly, when using this alternative parameter set. These observations suggested that the stress transmission and the micromechanical dissipation mechanisms (through particle-particle and particle wall collisions) might depend on the hopper angle.

4.3 Kinematic fields inside the hoppers

The numerical tool also allowed us to analyze bulk flow features in detail. Figure 11 illustrates, as color maps, the obtained spatial profiles of the vertical velocity $v_z(r, z)$. For comparison, findings corresponding to several hopper angles (α from $90° to 20°$) are displayed. As expected, in all cases, the velocity of the flow was faster in the region of the orifice, and it diminished to a significantly smaller value, when getting far from there, monotonically. However, the fast dynamics at orifice perturbed the rest of the system distinctly, depending on the angle of the hopper. Interestingly, small and large angles showed larger zone of influence in comparison with intermediate angles.

Figure 12 displays color maps, illustrating the spatial packing fraction profiles $\phi(r, z)$ obtained for different hopper angles α. In general, the packing fraction inside the bins resulted roughly constant $\phi_b \approx 0.58$. In the region of the orifice, however, the system was significantly more diluted, which correlated with a faster dynamics and higher granular temperature. Similarly to the velocity profiles, the packing fraction profiles also showed that the perturbation distance of the orifice seems to depend non-monotonically on α.

In Fig. 13a, we analyze the specific features of the velocity profiles on the vertical direction $v_z(r, z = h)$, at specific locations ($h = [2R, 3R, 5R, 10R]$) and obtained for the case $\alpha = 90$ (flat silo). Here our aim was to clarify

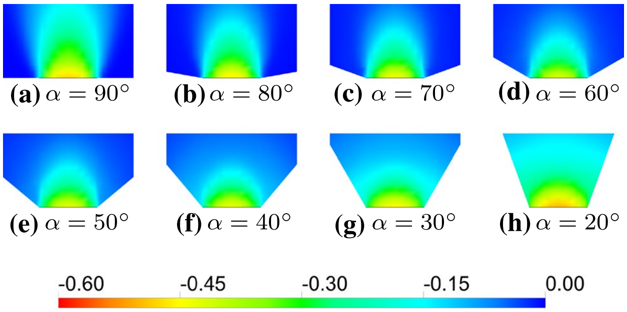

Fig. 11 Color-maps of vertical velocity, $v_z(r, z)$, for different hopper angles, α from 90° to 20°)

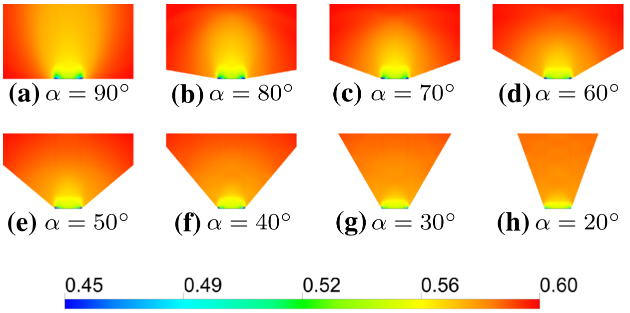

Fig. 12 Color-maps of solid-fraction, ϕ, for different hopper angles, α from 90° to 20°). Notice that fall arch shape changes with hopper angle, α. This shape is related with geometry, properties of material, and boundary conditions

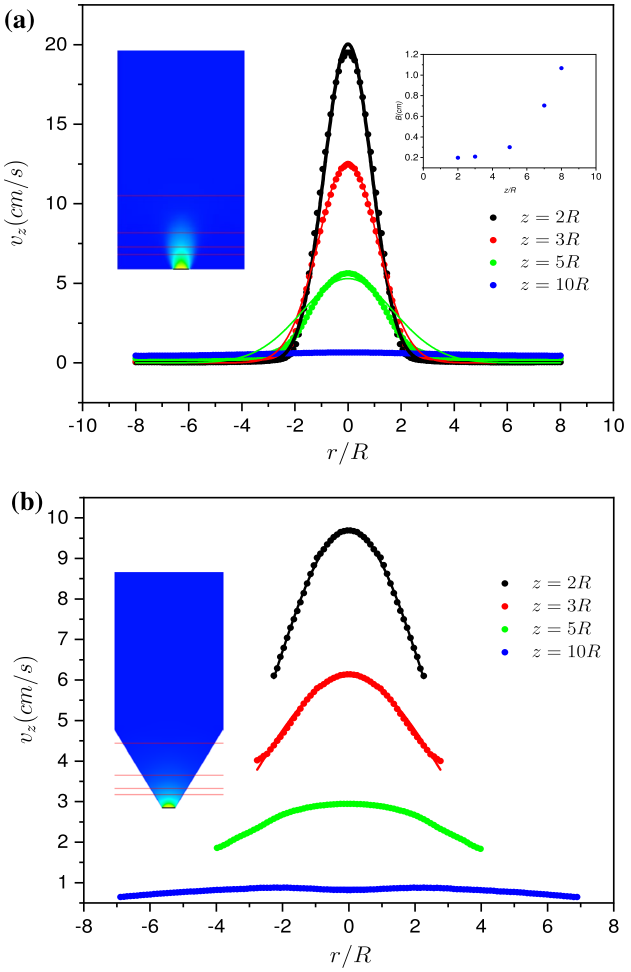

Fig. 13 Comparison of the spatial velocity profiles $v_z(x, z = h)$, obtained at different heights $h = [2R, 3R, 5R, 10R]$. To different cases are displayed, in a) ($r = 10$ mm, $\alpha = 90°$) and in **b** ($r = 10$ mm, $\alpha = 30°$)

possible correlations between the micromechanical features of the discharged material with the mass flow rate delivered through the system outlet. Decades ago, Nedderman and Tüzün [45] introduced a kinematic model, proposing that inside a silo the grain radial velocity v_r is proportional to the gradient of vertical velocity v_z along the radial direction. Thus, assuming that the granular material behaves as an incompressible fluid, they predicted a Gaussian velocity profile

$$v_z(r, z) = \frac{Q}{4\pi B z} \exp\left(-\frac{r^2}{4Bz}\right) \tag{11}$$

where Q is the mass flow rate at the orifice and B is a constant with length dimensions. In Fig. 13, several velocity profiles $v_z(r, z = h)$ are illustrated, and compared with Eq. (11) using B as a fitting constant. Note that the consistency of the outcomes was remarkable. Very recently it was found in a quasi-2D experiment [46, 47] that the value B increases with height, and here we found a similar trend.

Figure 13b illustrates the velocity profiles $v_z(r, z = h)$, obtained at specific locations (heights) for the case $\alpha = 30°$. Once again, the flow was slower at points located at higher locations, and practically diminished inside the hopper. Interestingly, at locations far from the orifice, the velocity profiles still showed a Gaussian shape in agreement the kinematic model of Eq. (11). Near to the orifice, however, a more liquid-like parabolic velocity profile was detected. Remark that the exact location of where this trend changes depended strongly on the hopper angle, as well as the rest of the model parameters.

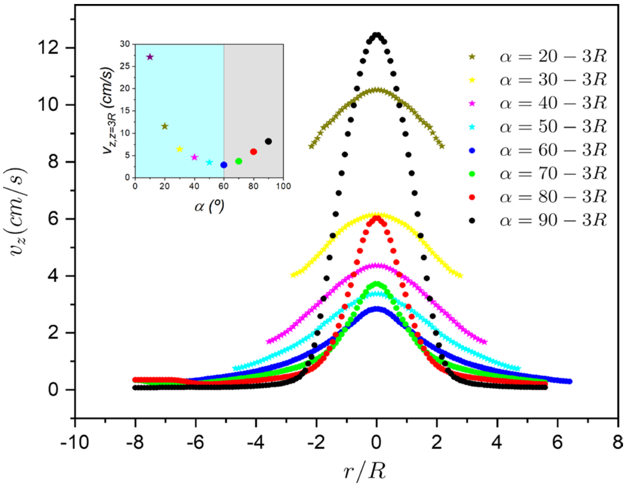

Fig. 14 Comparison of the spatial velocity profiles, $v_z(r, z = 3R)$ obtained at $z = 3R$, for the same orifice ($r = 10$ mm). For comparison, outcomes corresponding to different angles are illustrated (α from 90° to 20°). The inset shows the velocity at the center $v_z(r = 0, z = 3R)$ as a function of the hopper angle

The influence of the hopper angle on the kinetic fields inside the hoppers is examined in Fig. 14. For comparison, outcomes of $v_z(r, z = 3R)$ corresponding to different angles are illustrated. Note, that for large angles $\alpha > 50°$, the profiles were in good agreement with the predictions of the kinematic model of Eq.(11), and deviated from it for small hopper angles. The inset of Fig. 14 shows the velocity at the center $v_z(r = 0, z = 3R)$ as a function of the hopper angle α. Interestingly, we obtained that the velocity at the center of the hopper changes non-monotonically with the angle. This trend was also observed when examining the vertical velocity profiles at the orifice, and it correlates with the non-monotonotonic relationship of the particle flow rate with the angle.

Summarizing: we reported experimental and numerical results of granular flows in silos. Specifically, we explored experimentally the influence of the hopper angle α in determining the mass flow rate W, testing the entire domain of α, *i.e.* ranging from $\alpha = 10°$ to $\alpha = 90°$ (flat silo limit). In addition, the granular flow was also reproduced numerically using Computational Fluid Dynamics (CFD). The numerical implementation was validated, comparing the W values with experimental data obtained for several exit sizes. Thus, the most relevant parameters of the model were set, and used examining the flow rate dependence on α. Stepping forward, the velocity and density profiles obtained numerically for different hopper angles were also rationalized, employing a theoretical scheme that is based on their self-similar properties. Its outcome was the phenomenological expression (Eq. (7)), which relates the values of W with the solid fraction and vertical velocity profiles at the silo exit. Remarkably, this theoretical procedure is done without any artifacts like the *empty anulus*, which is commonly used to fit the experimental data when using Beverloo's correlation. In general, we found a good quantitative agreement of numerical and experimental results for the mass flow rate, analyzing the full range of explored hopper angles using a single set of the model parameters. The numerical tool even reproduced the weak non-monotonous behavior of the flow rate versus the hopper angle, that was obtained experimentally. However, for $\alpha > 50°$ and approaching to the flat silo limit, deviations between the numerical and experimental results were detected. In addition, we proposed a new collection of the model parameters, which reproduced these specific conditions. Unfortunately, for $\alpha < 50°$ the alternative approach became numerically unstable or underestimated the experimental results significantly. These observations suggested that both the macroscopic stress transmission and the micromechanical dissipation mechanisms (through particle-particle and particle-wall collisions) might depend on the hopper angle. It is worth mentioning that a similar analysis could be executed using a continuous formulation based on the concepts of the $\mu(i)$-rheology. These issues will be explored elsewhere.

Acknowledgements This work was funded by Ministerio de Economía y Competitividad (Spanish Government) through Projects No. FIS2017-84631-P, MINECO/AEI/FEDER, UE.

Compliance with ethical standards

Conflict of interest The authors declare that they have no conflict of interest, and the work is original and have not been published elsewhere in any form or language.

References

1. Nedderman, R.M.: Statics and Kinematics of Granular Materials. Cambridge University Press, Cambridge (1992)
2. Forterre, Y., Pouliquen, O.: Flows of dense granular media. Ann. Rev. Fluid Mech. **40**(1), 1–24 (2008)
3. Andreotti, B., Forterre, Y., Pouliquen, O.: Granular Media: Between Fluid and Solid. Cambridge University Press, Cambridge (2013)
4. Bagnold, R.A.: Experiments on a gravity-free dispersion of large solid spheres in a Newtonian fluid under shear. Proc. R. Soc. London Ser. A Math. Phys. Sci. **225**(1160), 49–63 (1954)
5. Chapman, S., Cowling, T.G.: *The mathematical theory of non-uniform gases: an account of the kinetic theory of viscosity, thermal conduction and diffusion in gases*. Cambridge, Eng.: Cambridge University Press, 3rd ed ed., (1970)
6. Savage, S.B., Sayed, M.: Gravity flow of coarse cohesionless granular materials in conical hoppers. Zeitschrift für angewandte Mathematik und Physik ZAMP **32**(2), 125–143 (1981)
7. Jenkins, S.S.J., Jenkins, J.T., Savage, S.B.: A theory for the rapid flow of identical, smooth, nearly elastic, spherical particles. J. Fluid Mech. **130**, 187–202 (1983)
8. Lun, C.K.K., Savage, S.B., Jeffrey, D.J., Chepurniy, N.: Kinetic theories for granular flow: inelastic particles in couette flow and slightly inelastic particles in a general flowfield. J. Fluid Mech. **140**, 223–256 (1984)
9. Gidaspow, D., Bezburuah, R., Ding, J.:"Hydrodynamics of circulating fluidized beds: kinetic theory approach," tech. rep., Illinois Inst. of Tech., Chicago, IL (United States). Dept. of Chemical, (1991)
10. Johnson, P.C., Jackson, R.: Frictional-collisional constitutive relations for granular materials, with application to plane shearing. J. Fluid Mech. **176**, 67–93 (1987)
11. Syamlal, M., Rogers, W., O'Brien, T.J.: "Mfix documentation: Volume 1, theory guide," *National Technical Information Service, Springfield, VA*, (1993)
12. Gidaspow, D.: Multiphase Flow and Fluidization: Continuum and Kinetic Theory Descriptions. Academic press, Cambridge (1994)
13. Benyahia, S.: Validation study of two continuum granular frictional flow theories. Ind. Eng. Chem. Res. **47**(22), 8926–8932 (2008)
14. Staron, L., Lagrée, P.-Y., Popinet, S.: The granular silo as a continuum plastic flow: the hour-glass vs the clepsydra. Phys. Fluids **24**(10), 103301 (2012)
15. Dunatunga, S., Kamrin, K.: Continuum modelling and simulation of granular flows through their many phases. J. Fluid Mech. **779**, 483–513 (2015)
16. Zheng, Q., Xia, B., Pan, R., Yu, A.: Prediction of mass discharge rate in conical hoppers using elastoplastic model. Powder Technol. **307**, 63–72 (2017)
17. Zhou, Y., Lagrée, P.-Y., Popinet, S., Ruyer, P., Aussillous, P.: Experiments on, and discrete and continuum simulations of, the discharge of granular media from silos with a lateral orifice. J. Fluid Mech. **829**, 459–485 (2017)
18. Luo, Q., Zheng, Q., Yu, A.: Quantitative comparison of hydrodynamic and elastoplastic approaches for modeling granular flow in silo. AIChE J. **65**(5), e16533 (2019)
19. Fullard, L., Holland, D.J., Galvosas, P., Davies, C., Lagrée, P.-Y., Popinet, S.: Quantifying silo flow using MRI velocimetry for testing granular flow models. Phys. Rev. Fluids **4**(7), 074302 (2019)
20. Zhou, Y., Lagrée, P.-Y., Popinet, S., Ruyer, P., Aussillous, P.: Gas-assisted discharge flow of granular media from silos. Phys. Rev. Fluids **4**(12), 124305 (2019)
21. Beverloo, W.A., Leniger, H.A., Van de Velde, J.: The flow of granular solids through orifices. Chem. Eng. Sci. **15**(3–4), 260–269 (1961)
22. Mankoc, C., Janda, A., Arevalo, R., Pastor, J.M., Zuriguel, I., Garcimartín, A., Maza, D.: The flow rate of granular materials through an orifice. Granul. Matter **9**(6), 407–414 (2007)
23. Aguirre, M.A., Grande, J.G., Calvo, A., Pugnaloni, L.A., Géminard, J.-C.: Granular flow through an aperture: pressure and flow rate are independent. Phys. Rev. E **83**(6), 061305 (2011)
24. Janda, A., Zuriguel, I., Maza, D.: Flow rate of particles through apertures obtained from self-similar density and velocity profiles. Phys. Rev. Lett. **108**(24), 248001 (2012)
25. Rubio-Largo, S.M., Janda, A., Maza, D., Zuriguel, I., Hidalgo, R.C.: Disentangling the free-fall arch paradox in silo discharge. Phys. Rev. Lett. **114**(23), 238002 (2015)
26. Koivisto, J., Durian, D.J.: The sands of time run faster near the end. Nat. commun. **8**(1), 1–6 (2017)
27. Darias, J., Madrid, M.A., Pugnaloni, L.A.: Differential equation for the flow rate of discharging silos based on energy balance. Phys. Rev. E **101**(5), 052905 (2020)
28. Huang, X., Zheng, Q., Yu, A., Yan, W.: Shape optimization of conical hoppers to increase mass discharging rate. Powder Technol. **361**, 179–189 (2020)
29. Danczyk, M., Meaclem, T., Mehdizad, M., Clarke, D., Galvosas, P., Fullard, L., Holland, D.: Influence of contact parameters on discrete element method (dem) simulations of flow from a hopper: Comparison with magnetic resonance imaging (mri) measurements. Powder Technol. **372**, 671–684 (2020)
30. Huang, X., Zheng, Q., Yu, A., Yan, W.: Optimised curved hoppers with maximum mass discharge rate—an experimental study. Powder Technol. **377**, 350–360 (2021)
31. Brown, R.: Minimum energy theorem for flow of dry granules through apertures. Nature **191**(4787), 458 (1961)
32. Darias, J., Gella, D., Fernández, M., Zuriguel, I., Maza, D.: The hopper angle role on the velocity and solid-fraction profiles at the outlet of silos. Powder Technol. **366**, 488–496 (2020)
33. ANSYS, Inc, *ANSYS Fluent Theory Guide*, (2018)
34. Ng, B.H., Ding, Y., Ghadiri, M.: "Assessment of the kinetic–frictional model for dense granular flow," *Particuology*, vol. 6, no. 1, pp. 50 – 58, (2008). Selected papers from 1st UK-China Particle Technology Forum
35. Busch, A., Johansen, S.T.: On the validity of the two-fluid-ktgf approach for dense gravity-driven granular flows as implemented in ansys fluent r17.2. Powder Technol. **364**, 429–456 (2020)
36. Schaeffer, D.G.: Instability in the evolution equations describing incompressible granular flow. J. Differ. Equ. **66**(1), 19–50 (1987)
37. Chialvo, S., Sundaresan, S.: A modified kinetic theory for frictional granular flows in dense and dilute regimes. Phys. Fluids **25**(7), 070603 (2013)

38. Johnson, P.C., Nott, P., Jackson, R.: Frictional—collisional equations of motion for participate flows and their application to chutes. J. Fluid Mech. **210**, 501–535 (1990)
39. Boemer, A., Qi, H., Renz, U.: Eulerian simulation of bubble formation at a jet in a two-dimensional fluidized bed. Int. J. Multiphase Flow **23**(5), 927–944 (1997)
40. Syamlal, M.: "A review of granular stress constitutive relations," tech. rep., EG and G Washington Analytical Services Center, Inc., Morgantown, WV (USA), 1 (1987)
41. Wachem, B. G. M., van, Schouten, J. C., Krishna, R., Bleek, C. M., van den: "Comparative analysis of CFD models for dense gas-solid systems. In: *Proc. of the AIChE 1999 Annual Meeting, Fluidization and Fluid-Particle Systems* (L. Glicksman, ed.), p. 79, (1999)
42. D. Fletcher, Mcclure, D., Kavanagh, J., Barton, G.: "Cfd Simulation of Industrial Bubble Columns : Numerical and Modelling Challenges and Successes. In: *11th International Conference on CFD in the Minerals and Process Industries*, vol. 3, no. December, pp. 1–6, (2015)
43. Rubio-Largo, S., Maza, D., Hidalgo, R.C.: Large-scale numerical simulations of polydisperse particle flow in a silo. Comp. Part. Mech. **4**, 419–427 (2017)
44. Brown, R.L., Richards, J.C.: Principles of Powder Mechanics: Essays on the Packing and Flow of Powders and Bulk Solids, vol. 10. Elsevier, Amsterdam (2016)
45. Nedderman, R., Tüzün, U.: A kinematic model for the flow of granular materials. Powder Technol. **22**(2), 243–253 (1979)
46. Zuriguel, I., Maza, D., Janda, A., Hidalgo, R.C., Garcimartín, A.: Velocity fluctuations inside two and three dimensional silos. Granul. Matter **21**, 47 (2019)
47. Choi, J., Kudrolli, A., Bazant, M.Z.: Velocity profile of granular flows inside silos and hoppers. J. Phys. Condens. Matter **17**, S2533–S2548 (2005)